Loading rate effects on dynamic failure of quasi-brittle solids: Simulations with a two-scale damage model

Megbeme Komla Atiezo, Wen Chen, Cristian Dascalu

To cite this version:

Megbeme Komla Atiezo, Wen Chen, Cristian Dascalu. Loading rate effects on dynamic failure of quasi-brittle solids: Simulations with a two-scale damage model. Theoretical and Applied Fracture Mechanics, 2019, 100, pp.269-280. ⟨10.1016/j.tafmec.2019.01.011⟩. ⟨hal-02915370⟩

Version of Record: https://www.sciencedirect.com/science/article/pii/S0167844218303471
Manuscript_5c37196e19a223d9e12c7d94ee302b62

Loading rate effects on dynamic failure of quasi-brittle solids : simulations with a two-scale damage model

Megbeme Komla Atiezo, Wen Chen, Cristian Dascalu
Université de Lorraine, CNRS, Arts et Métiers ParisTech, LEM3, F-57000 Metz, France

---

Abstract

In this contribution we present numerical simulations of rapid failure in brittle materials using a dynamic damage law. The model is deduced from a microscopic Griffith-type criterion describing the dynamic mode I propagation of microcracks, using a homogenization method based on asymptotic expansions. The resulting damage law is sensitive to the loading rate that influences the macroscopic failure modes. Finite Element simulations are performed in order to identify the model predictions and the obtained numerical results are compared with the experimental ones. Compact tension and L-shape specimen tests for concrete materials, compact compression test for the PMMA brittle polymers and Kalthoff impact test for limestone rocks are considered in the numerical simulations. We show that the loading rate essentially determines the macroscopic crack trajectory and the associated branching patterns. The obtained results are in good agreement with those reported in the experimental works.

Keywords: Micro-cracks, two-scale damage law, dynamic failure,
loading-rate effects, Finite Element simulations, quasi-brittle materials

---

Preprint submitted to Elsevier *2 décembre 2018*

1. Introduction

In the last decades, many experimental, numerical and theoretical works have been published on the dynamic failure of quasi-brittle materials (e.g., Reinhardt, 1982; Banthia et al., 1987; Larcher, 2009; Ozbolt et al., 2012; Freund, 1998; Bischoff et al., 1991; Ozbolt et al., 2006; Bede et al., 2015; Malvar and Ross, 1998; Klepaczko et al., 2001; Brara and Klepaczko, 2006; Weerheijm and Van Doormaal, 2007; Forquin and Erzar, 2010; Erzar and Forquin, 2014).

For the mode I fracture of concrete, most of the experimental works focused on the strain-rate dependance of the tensile strength, mainly by using indirect methods such as split Hopkinson bar tests leading to spalling failure after reflection of the initial compression wave at the free end of the specimen (e.g., Malvar and Ross, 1998; Klepaczko et al., 2001; Brara and Klepaczko, 2006; Weerheijm and Van Doormaal, 2007; Forquin and Erzar, 2010; Erzar and Forquin, 2014). However, in more general tests the rate of loading not only influences the tensile strength but also the fracture mode by inducing different crack trajectories or multi-branches crack systems.

For concrete specimens, the compact tension and L-specimen experiments performed by Ozbolt et al. (2013, 2015) indicate that the increase of the loading speed changes the failure paths showing pronounced deviations from the quasi-static propagation direction and the formation of multiple branches. Rittel and Maigre (1996a,b) used the compact compression specimen test to characterize the initial kink angle and the dynamic fracture toughness of PMMA under transient loading. The authors showed that the initial kink angle increases with impact velocity. The classical Kalthoff's test leading to mode I failure under shear impact loading has been used by Bertram and Kalthoff (2003); Bertram (2008) for brittle limestone rocks. A specific development of multi-branches crack system is observed at high loading rates. The aim of the present contribution is to reproduce all these experimental results using a recently proposed dynamic damage model of microstructural origin.

Despite the important advancements achieved during the last decades by the Fracture Mechanics approaches, they still remain difficult to apply for the modeling of complex multi-crack systems. The distributed damage models are particularly interesting for this task. Rate-dependent viscous-type damage laws has been proposed, for instance, by Dubé et al. (1996); Allix et al. (2003)). Efforts have been done to construct damage evolution models accounting for microstructural evolutions, like those proposed by Fanella et al. (1988); Ren et al. (2011); Kirane et al. (2015).

It is known that the propagation of the microcracks plays an essential role in the failure of quasi-brittle materials like concrete and rocks. This motivates the construction of multiscale damage models based on explicit evolutions of microcracks. Such a dynamic damage law has been proposed in Keita et al. (2014); Dascalu (2018) to predict the rapid failure of brittle materials. The model is deduced from evolving microstructures consisting of microcracks propagating dynamically, in mode I, by adapting the asymptotic homogenization method (Dascalu et al., 2008).

This dynamic two-scale damage model is adopted in the present contribution to reproduce the experiments reported in Ozbolt et al. (2013, 2015); Rittel and Maigre (1996a); Bertram and Kalthoff (2003). Finite Element simulations of these tests are performed and the results are compared with the experimental ones, with special emphasis on the loading rate effects on dynamic failure modes. It will be shown that all these experimental results concerning different types of loading rate effects on fracture can be successfully simulated with the adopted damage model.

The paper is organized as follows. In Section 2, the dynamic damage model is presented. Subsequently, the results of the numerical simulations are presented for the four tests in Sections 3-6, respectively. General conclusions are finally formulated.

2. Two-scale damage model

In this section we give the basic equations of the dynamic elasto-damage model. For details concerning the homogenization procedure leading to the macroscopic damage law presented here, the reader is referred to Keita et al. (2014) and Dascalu (2018).

All the mechanical fields are assumed to depend on the space variables x_1, x_2, x_3 and the time t. The equations at the macroscopic scale are obtained using the asymptotic homogenization method for a locally periodic micro-fractured medium. The elementary period is a square of size ε that contains one centered traction-free microcrack of length l and the damage variable is defined as the normalized length $d = l/\varepsilon$, also representing the length of a microcrack in a unit cell. The small-scale local periodicity assumption allows for spatial variations of the macroscopic variable $d(x_i, t)$, corresponding to smooth variations of the microscopic crack length l with fixed period size ε.

To formulate the initial multi-crack problem, we denote by $\sigma^{\varepsilon}_{ij}$ the stress field and by u_i^ε the displacement field. The momentum balance equations are :

$$\frac{\partial \sigma_{ij}^\varepsilon}{\partial x_j} = \rho \frac{\partial^2 u_i^\varepsilon}{\partial t^2} \tag{1}$$

and the linear elasticity constitutive relations :

$$\sigma_{ij}^\varepsilon = a_{ijkl} e_{kl}(\mathbf{u}^\varepsilon) \tag{2}$$

where the linearized strain tensor is $e_{ij}(\mathbf{u}^\varepsilon) = \frac{1}{2}\left(\frac{\partial u_i^\varepsilon}{\partial x_j} + \frac{\partial u_j^\varepsilon}{\partial x_i}\right)$. For an isotropic, homogeneous solid, the linear elasticity tensor has the form $a_{ijkl} = \frac{\nu E}{(1+\nu)(1-2\nu)}\delta_{ij}\delta_{kl} + \frac{E}{2(1+\nu)}(\delta_{ik}\delta_{jl} + \delta_{il}\delta_{jk})$, where E is the Young modulus, ν is the Poisson ratio and δ_{ij} is the Kronecker symbol.

On microcracks boundaries, traction-free conditions are assumed :

$$\sigma_{ij}^\varepsilon N_j = 0 \tag{3}$$

where N_j are the components of the unit normal vector on the crack faces. Periodicity conditions are assumed on the outer boundaries of the cells of size ε. After the use of the asymptotic developments, in the unit cell problem crack-face type loadings are present depending on the macroscopic deformation (Dascalu et al., 2008; Keita et al., 2014). These conditions are equivalent with those of periodicity via an imposed macroscopic strain. When the microcracks are approaching the cell boundaries we can reasonable assume that the failure occurs in the corresponding macroscopic point.

The application of the asymptotic homogenization method (Dascalu et al., 2008; Keita et al., 2014) lead to the macroscopic equation of motion

$$\frac{\partial \sigma_{ij}}{\partial x_j} = \rho \frac{\partial^2 u_i}{\partial t^2} \tag{4}$$

and the homogenized stress-strain law

$$\sigma_{ij} = C_{ijkl}(d)e_{kl}(\mathbf{u}) \tag{5}$$

for the macroscopic displacement $u_i(x_j, t)$ and damage $d(x_j, t)$ fields, with the effective coefficients C_{ijkl} depending on the damage variable d.

In the previous works (Dascalu et al., 2008; François and Dascalu, 2010; Dascalu et al., 2010; Wrzesniak et al., 2015; Dobrovat et al., 2015) the coefficients $C_{ijkl}(d)$ were obtained by computations on the unit cell containing a single crack and with periodic boundary conditions. The particular orientation of microcracks lead to damage induced anisotropy and, as shown in Dascalu et al. (2008), for $d = 1$ the normal stiffness vanishes as the consequence of the coalescence of micro-cracks in the periodic system.

In the present contribution we will adopt the classical expression of Damage Mechanics as the linear approximation of $C_{ijkl}(d)$:

$$C_{ijkl}(d) = (1 - d)^{\alpha} a_{ijkl} \tag{6}$$

where a_{ijkl} are the elastic coefficients of the virgin material, assumed to be homogeneous and isotropic. In all the simulations presented in the following chapters, the specimens can be considered as macroscopically isotropic, with microcracks developing in various directions at the small scale. For special cases, like those of stratified materials, anisotropic response should be assumed as a consequence of preferential directions of microcrack evolution.

The propagation of microcracks is described at the macroscale by the evolution in time of the damage variable $d(x_i, t)$ at a given material point. In order to obtain a damage evolution law, a specific approach has been proposed in (Dascalu et al., 2008; François and Dascalu, 2010; Keita et al., 2014;

Dascalu, 2018) starting from a Griffith-type microscopic fracture criterion involving the dynamic energy release rate at the microcrack tips (Freund, 1998) :

$$\mathcal{G}^{d\varepsilon} = \lim_{r \to 0} \int_{\Gamma_r} (U+T)n_1 - \sigma^{\varepsilon}_{ij} n_j \frac{\partial u^{\varepsilon}_i}{\partial x_1} \, dS \tag{7}$$

where

$$U = \frac{1}{2} a_{mnkl} e_{kl}(\mathbf{u}^{\varepsilon}) e_{mn}(\mathbf{u}^{\varepsilon}) \quad ; \quad T = \frac{1}{2} \rho \frac{\partial \mathbf{u}^{\varepsilon}}{\partial t} \frac{\partial \mathbf{u}^{\varepsilon}}{\partial t} \tag{8}$$

are respectively the elastic and the kinetic energy densities. Here Γ_r is a circle of an infinitesimal radius r surrounding the crack tip and $\mathbf{n}$ is the outward unit normal on the cercle Γ_r.

The microcrack propagation is assumed to be symmetrical with respect to the center of each period and it occurs when the energy-release rate $\mathcal{G}^{d\varepsilon}$ reaches the critical fracture energy $\mathcal{G}_c$ of the material. More precisely, the evolution of microcracks is gouverned by the following relations :

$$\mathcal{G}^{d\varepsilon} \leq \mathcal{G}_c \ ; \ \frac{dl}{dt} \geq 0 \ ; \ \frac{dl}{dt}(\mathcal{G}^{d\varepsilon} - \mathcal{G}_c) = 0 \tag{9}$$

Using the homogenization approach proposed in Keita et al. (2014); Dascalu (2018) one obtains the following damage relation :

$$\dot{d} \left(\frac{1}{2} \frac{dC_{ijkl}(d)}{dd} e_{xkl}(\mathbf{u}) e_{xij}(\mathbf{u}) + \frac{\mathcal{G}_c}{\varepsilon g(v)} \right) = 0 \tag{10}$$

The universal function $g(v)$ of the crack-tip speed v makes the link between the dynamic and the quasistatic energy release rates $\mathcal{G}^{d\varepsilon} = g(v)\mathcal{G}^{\varepsilon}$ and can be approximated by the formula (Freund, 1998) :

$$g(v) \approx (1 - \frac{v}{C_R}) \tag{11}$$

where C_R is the Rayleigh wave speed.

The velocity of the microcrack tips can be written as $v = \frac{d}{dt}(\frac{l}{2}) = \frac{\varepsilon}{2}\dot{d}$ and the combination with (11) in (10) leads to the dynamic damage evolution law :

$$\dot{d} = \frac{2C_R}{\varepsilon} \left\langle 1 + \frac{\mathcal{G}_c}{\frac{\varepsilon}{2}\frac{dC_{ijkl}(d)}{dd} e_{kl}(\mathbf{u}) e_{ij}(\mathbf{u})} \right\rangle \tag{12}$$

where $\langle . \rangle$ represents the positive part. If we introduce the damage energy-release rate $Y = -\frac{1}{2}\frac{dC_{ijkl}(d)}{dd} e_{kl}(\mathbf{u}) e_{ij}(\mathbf{u})$, then the evolution law reads :

$$\dot{d} = \frac{2C_R}{\varepsilon} \left\langle 1 - \frac{\mathcal{G}_c}{\varepsilon Y} \right\rangle \tag{13}$$

We note that thermodynamic compatibility is assured via the macroscopic free energy function $\Psi = \frac{1}{2}C_{ijkl}(d)e_{kl}(\mathbf{u})e_{ij}(\mathbf{u})$ as a potential for the associated fields

$$\sigma_{ij} = \frac{\partial \Psi}{\partial e_{kl}} \quad ; \quad Y = -\frac{\partial \Psi}{\partial d} \tag{14}$$

for the macroscopic stresses $\sigma_{ij} = C_{ijkl}(d)e_{kl}(\mathbf{u})$ and the damage energy-release rate Y defined before, with $C_{ijkl}(d) = (1-d)^{\alpha} a_{ijkl}$.

The damage law (13) contains the parameter ε. Its physical meaning is that of mutual distance between neighbor microcracks in the locally periodic system. The influence of ε on the macroscopic response has been illustrated and explained in details in previous works (Dascalu et al., 2008; Keita et al., 2014; Dascalu, 2017). To illustrate this dependency, in Fig. 1 the uniaxial stress-strain and damage-strain curves are given for three micro-structural lengths, with the parameter $\alpha = 1.4$. We note that for smaller values of ε the strength is increasing, the damage initiation is delayed and the behavior is more brittle.

It is important to note that in real specimens the distribution of microcracks is much more complex than the periodic one assumed for the construc-

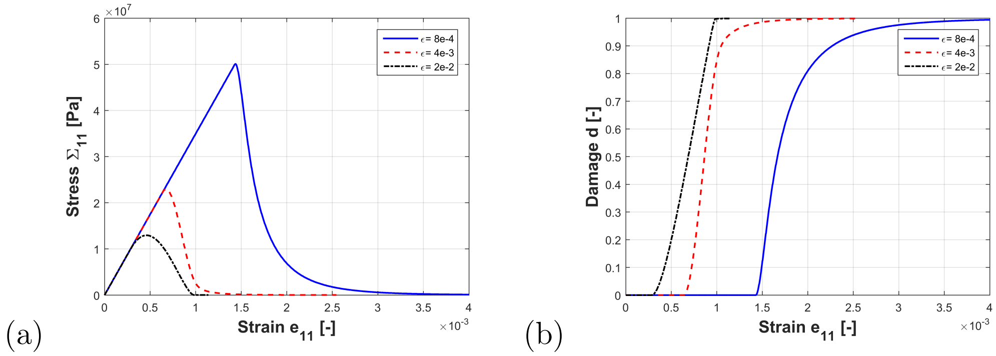

FIGURE 1: Stress (a) and damage (b) response for micro-structural lengths $\varepsilon = 8e - 4\,m$, $\varepsilon = 4e - 3\,m$ and $\varepsilon = 2e - 2\,m$.

tion of the model. In this case, the model has to be used with a "microscopic length of the equivalent periodic system" that would provide realistic damage evolutions. This implies calibrations of ε depending not only on the material but also on the geometry and the loading type of the specimen.

In the law (13) the volumetric energy release rate Y is driving the damage evolution and its expression is symmetric with respect to tension or compression deformations. To avoid physically unrealistic failure in compression, we consider only the positive part Y_+ in the equation (13). Following Miehe et al. (2010), we define the positive part of the energy-release rate as :

$$Y_+ = \alpha(1-d)^{\alpha-1}\left(\frac{E\nu}{2(1+\nu)(1-2\nu)}\,\langle tr[\mathbf{e}(\mathbf{u})]\rangle^2 + \frac{E}{2(1+\nu)}\,tr[\mathbf{e}_+(\mathbf{u})^2]\right) \quad (15)$$

with $\langle . \rangle$ the positive part and tr the trace operator. Here $\mathbf{e}_+(\mathbf{u})$ represents the positive strain tensor, corresponding to the positive parts of the principal strains in the spectral decomposition of $\mathbf{e}(\mathbf{u})$.

The particular expressions (6) of the effective coefficients combined with

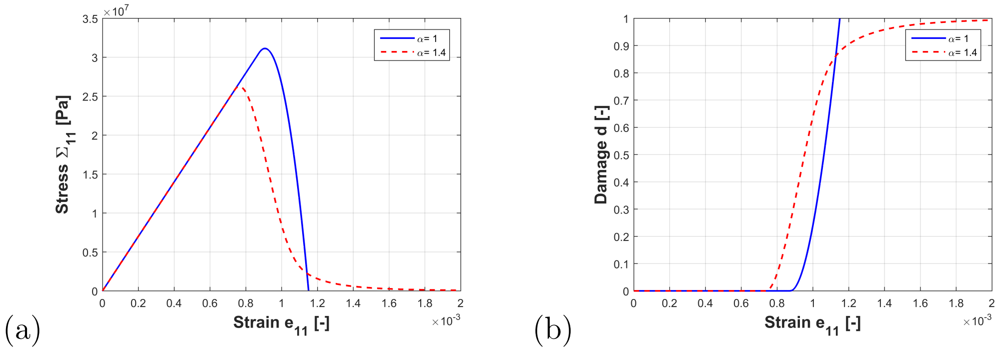

Figure 2: Stress-strain (a) and damage-strain (b) curves for two values of the exponent $\alpha = 1$ and $\alpha = 1.4$.

the homogenized damage law (13) assure an isotropic elasto-damage response. As concerns the parameter α, already introduced in Dascalu (2017), we illustrate in Fig. 2 its influence on the local macroscopic response predicted by the elasto-damage model. The stress and damage responses for a constant strain-rate uniaxial strain path are plotted for the exponent values α= 1 and α = 1.4. We note the influence on the post-peak response : while for α= 1 we get a more brittle response, for α = 1.4 the softening regime corresponds to a quasi-brittle behavior, with complete failure reached asymptotically. In the following sections, this last value will be used in the simulations for concrete and limestone while for the PMMA material the value α =1 will be considered.

In the next sections, the coupled elasto-damage system (4), (6), (13) and (15) will be numerically solved to reproduce dynamic failure tests.

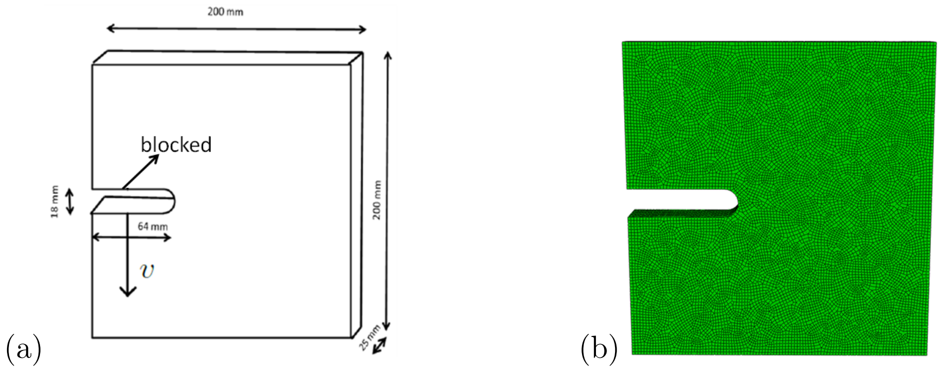

FIGURE 3: Geometry (a) and mesh (b) of the compact tension specimen.

3. Compact tension test

The Compact tension (CT) test is a classical experiment that can be used to determine the tensile strength of concrete. It is schematically represented in the Figure 3a. Under quasistatic loadings, a single crack is initiated at the pre-existing notch tip and propagates in the direction normal to that of the applied loading. At high loading rates, more complex failure modes are developed, as reported in Ozbolt et al. (2013). Our aim in this section is to numerically model the CT test using the previously described damage model and to analyze the loading rate influences on failure by comparison with the experimental results in Ozbolt et al. (2013).

The length, height and thickness of the specimen used in the compact tension test are $200\,mm$, $200\,mm$ and $25\,mm$, respectively. The specimen contains an initial notch of length $64\,mm$ and width $18\,mm$ with a rounded tip. The upper side of the notch is blocked, while a constant velocity v is applied on its lower side.

The material properties of concrete are those reported in the experiments :

Young's modulus $E = 36\,GPa$, Poisson's ratio $\nu = 0.18$, mass density $\rho = 2400\,kg/m^3$ and fracture energy $G_c = 65\,J/m^2$. For the present simulations, the appropriate value of the microstructural length has been found to be $\epsilon = 3\,mm$.

The two-scale damage model was implemented in the finite element code Abaqus Explicit (ABAQUS, 2013) through a VUMAT subroutine. The domain is discretized using linear, reduced-integration hexahedral elements. Fig. 3b shows a typical finite element mesh used for computations, with approximate element size of $1\,mm$.

The analysis in Dascalu (2017) showed that for the present model the damage localizes in regions of size of about the order of ε. To assure mesh objectivity we need to consider Finite Element meshes with element size smaller than the microstructural length and this will generally be the case in the simulations considered in the present contribution.

Three loading rates are considered : a) $v = 0.5\,m/s$, b) $v = 1.4\,m/s$ and c) $v = 3.3\,m/s$. In Fig. 4 the experimental results (left side) reported in Ozbolt et al. (2013) and the corresponding numerical simulations (right side) are presented. We note that for the velocity $v = 0.5\,m/s$, closer to the quasi-static regime, a single crack is formed starting from the tip of the notch and propagating in a direction approximately parallel to that of the notch.

When the rate of the applied displacement is increased to $v = 1.4\,m/s$, we observe that a curved fracture path is formed showing a general tendency of mode change from pure mode I to mixed mode propagation, with a shear component induced by the loading applied on the right face of the notch. It is important to remark that this mixed-mode rupture at the macroscopic level is

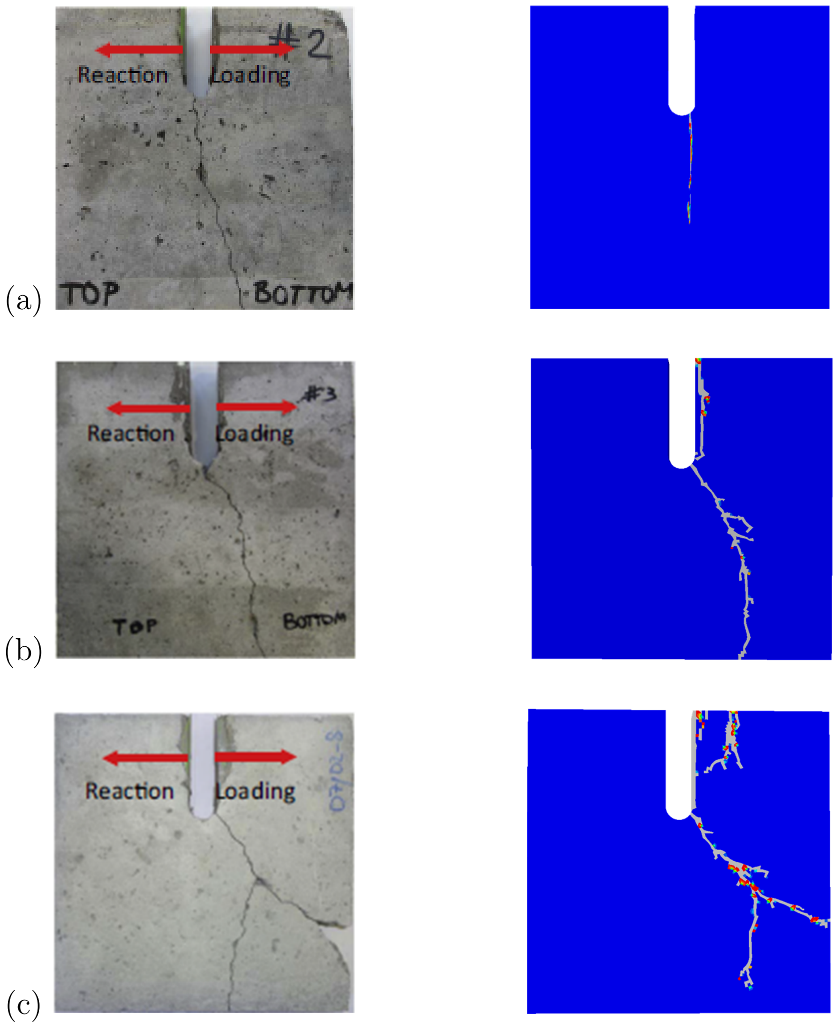

FIGURE 4: Experimental (left) and numerical (right) failure patterns for compact tension test corresponding to the loading velocities : (a) $v = 0.5\,m/s$, (b) $v = 1.4\,m/s$, (c) $v = 3.3\,m/s$

obtained using a damage model based essentially on the mode I propagation of microcracks.

Another specific feature of the rapid crack propagation retrieved in the

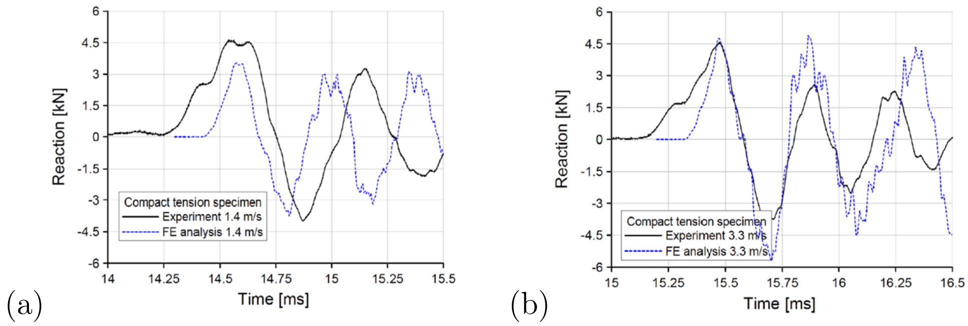

FIGURE 5: The reaction versus time response for displacement rates (a) $v = 1.40\,m/s$, (b)$v = 3.3\,m/s$, reproduced from Ozbolt et al. (2013).

case $v = 3.3\,m/s$ is the branching of the main crack. Micro-branching events are observed in the cases b) and c) as a result of the velocity increase (Dascalu, 2018) and are precursory to the macroscopic branching taking place at about half length of the main crack for $v = 3.3\,m/s$. We note that the numerical simulations follow closely the experimental observations concerning this particular fracture trajectory.

The results of the numerical simulations also show the development of secondary damage effects close to the notch side where the loading is applied. Such deterioration zones can be observed on the lips of the notch on the images of the physical specimens, with less important extend. Further analysis is necessary to determine how to control these effects, that will be also retrieved in the L-shaped test given in the next section. However, performed simulations with deactivation of the damage evolution in these areas showed similar results on the global failure evolution and dependency of the loading rate.

In Fig. 6, we represent the computed reaction on the fixed boundary of the notch as function of time. These results should be compared with the experimental ones (Ozbolt et al., 2013) reproduced in Fig. 5. We observe rather similar time evolutions of the reaction with agreement of the peak values for both applied velocities. We also remark that the peak value is increasing with the displacement rate.

The peak values of the reaction are compared in Fig. 7 with those obtained experimentally (Ozbolt et al., 2013), for the three applied velocities. The maximum reaction is plotted as a function of the corresponding displacement rate in logarithmic scale. The predicted evolution approaches the experimental values with a more rapid increase between $v = 0.5\,m/s$ and $v = 1.4\,m/s$ and differences of maximum $1kN$ between theory and experiment. One reason for the discrepancies between the measured and predicted values could be the fact that the complex loading system, with steel frames, used in (Ozbolt et al., 2013) has not been modeled numerically in the present simulations. For high values of the loading rate, the model predictions are more accurate, with even better calibration possibilities when restraining to these range of

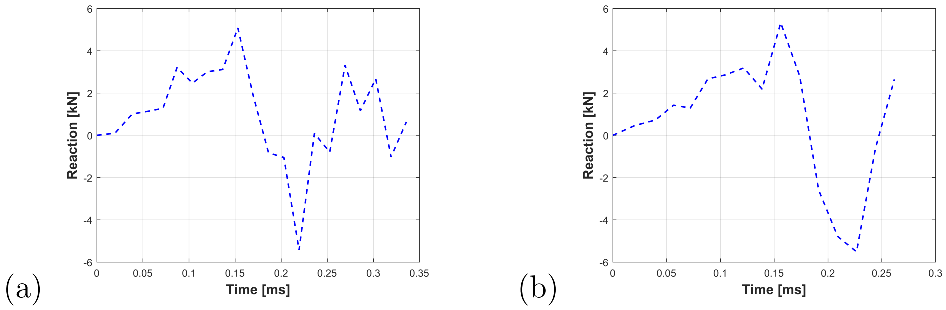

Figure 6: Numerical reaction versus time for displacement rates (a) $v = 1.40\,m/s$, (b) $v = 3.3\,m/s$.

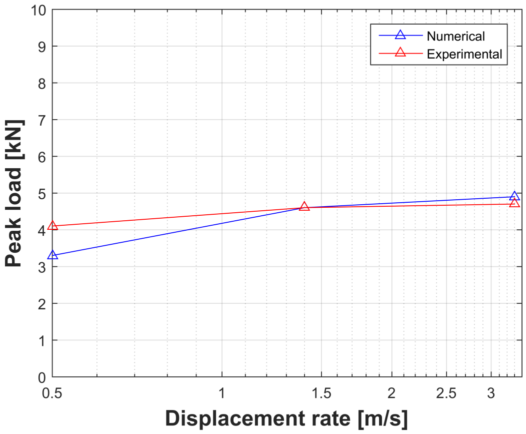

Figure 7: Numerical and experimental results for peak load at three loading rates of CT-test

applied velocities.

We finally address the question of the objectivity with respect to the finite element mesh. It is well-known that the rate-dependent models and, in particular, the viscous damage models introduce a regularizing effect and avoid pathological mesh dependency. For a more detailed study concerning the mesh objectivity of the present damage model we refer the reader to Dascalu (2017).

To illustrate the influence of the element size in the simulations for the Compact Tension test, we show in Fig. 8 the failure paths for two meshes having element sizes of $1\,mm$ and, respectively, $0.5\,mm$, in the case of loading velocity $v = 1.4\,m/s$. We can remark that the overall failure paths are quite similar, with slightly modified trajectories and more pronounced branching effects in the case of the refined mesh. The later effect can be understood in the light of branching instabilities and the triggering role of the FE mesh, as

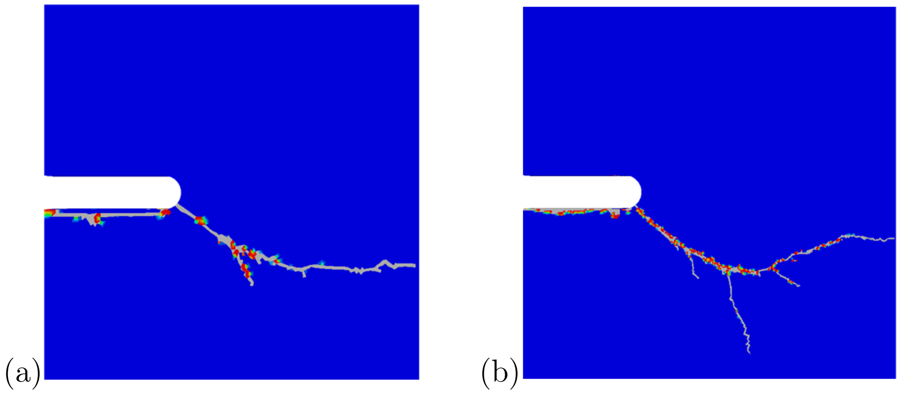

FIGURE 8: Compact tension test : simulations with FE meshes of a) element size $= 1\,mm$ and b) element size $= 0.5\,mm$.

discussed in Dascalu (2018). The comparison of the peak loads with the ones presented in Fig. 7 also revealed good agreement.

4. L-shaped specimen test

The second example we consider is the L-specimen test for concrete, as described by Ozbolt et al. (2015). The geometry the L-shaped block of width $500\,mm$, height $500\,mm$ and thickness $50\,mm$ is illustrated in Fig. 9a. A vertical displacement is progressively applied, at constant rate v, on a circular area of diameter $30\,mm$ at the bottom free side of the specimen (arrow in Fig. 9a), which center is situated at $30\,mm$ distance of to the left edge. Rectangular bottom regions on the front and back sides are blocked, they are represented in red color in Fig. 9a.

The concrete material parameters are those reported in the experiments : Young's modulus $E = 32.2\,GPa$, Poisson's ratio $\nu = 0.18$, mass density $\rho = 2210\,kg/m^3$ and fracture energy $G_c = 58.5\,J/m^2$. The microstructural

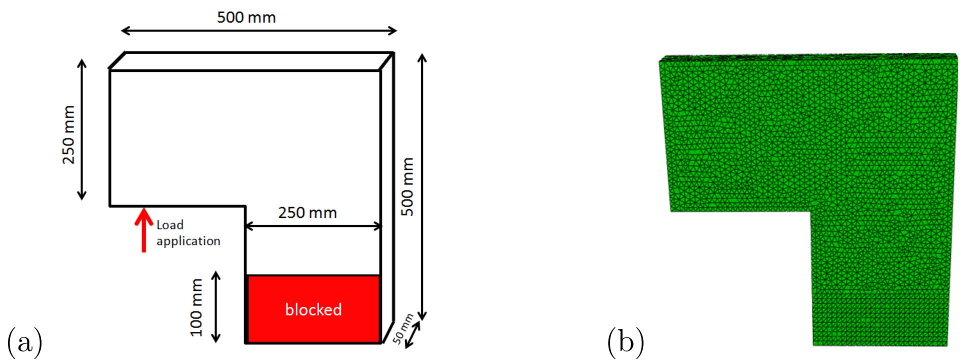

FIGURE 9: Geometry, dimensions, loading (a) and FE mesh (b) for the L-shaped concrete specimen.

length has been calibrated to $\epsilon = 0.006\,m$. Finite Element computations are performed with ABAQUS software. The domain is discretized with linear displacement tetrahedral elements which size is about $2.5\,mm$. A typical FE mesh used is shown in Fig. 9b.

Four loading rates are considered in the numerical simulations : a) $v = 0.35\,m/s$, b) $v = 0.74\,m/s$, c) $v = 1.1\,m/s$ and d) $v = 2.4\,m/s$. The fractured specimens obtained in the experiments (Ozbolt et al., 2015) and the corresponding ones resulting from computations with the present model are presented in Fig. 10.

As observed in the experiments, for low displacement rates a single crack is formed starting from the interior corner and, after a partial advancement in the diagonal direction, it tends to approach the direction normal to the applied loading. This corresponds to the classical mode I opening and it is retrieved in the numerical simulations. In the last regime, just before percolation, the numerical solution becomes highly unstable with a tendency of

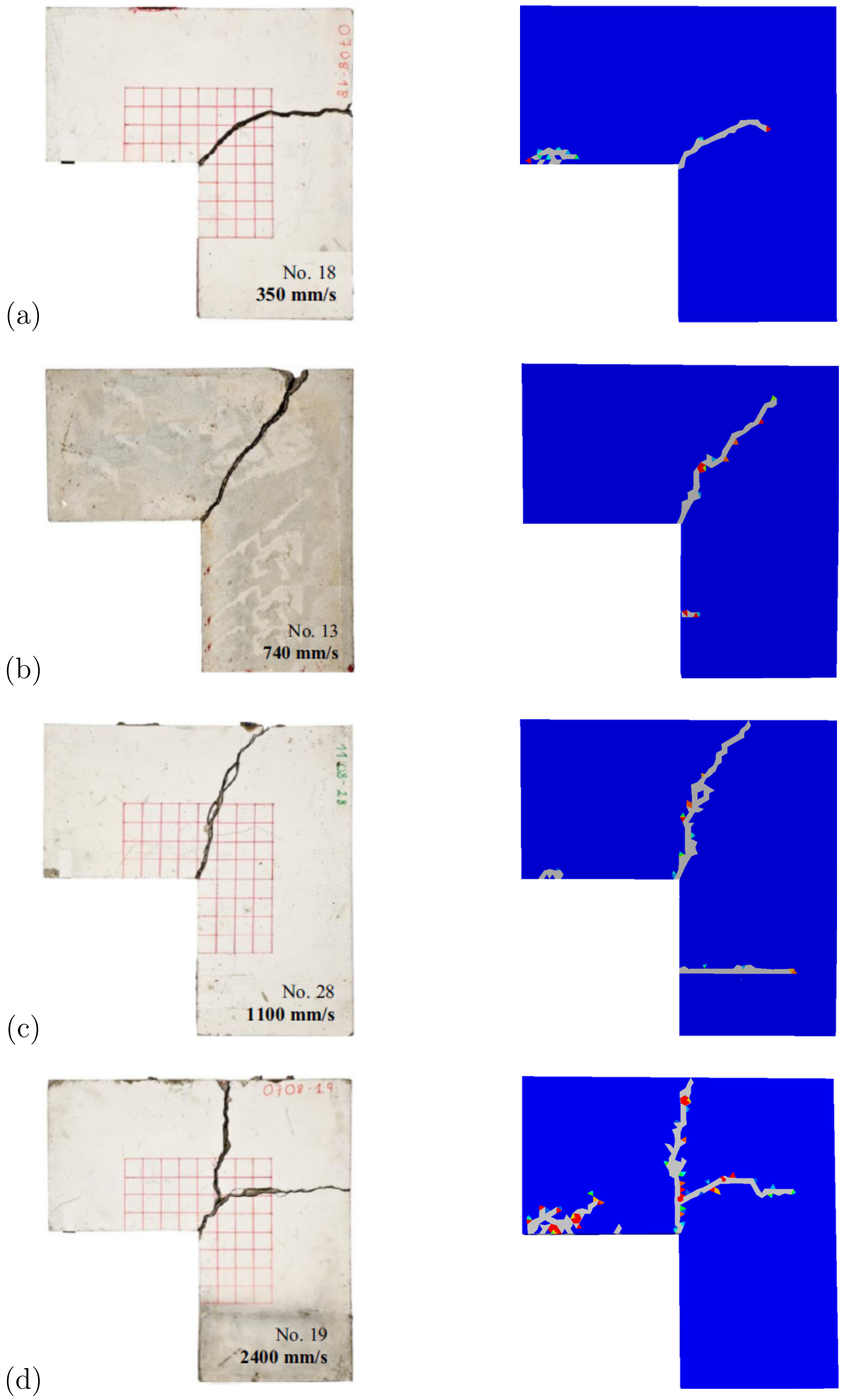

Figure 10: Experimental (left) and numerical (right) failure patterns for the L-specimen test for loading velocities : (a) $v = 0.35\,m/s$, (b) $v = 0.74\,m/s$, (c) $v = 1.1\,m/s$ and (d) $v = 2.4\,m/s$.

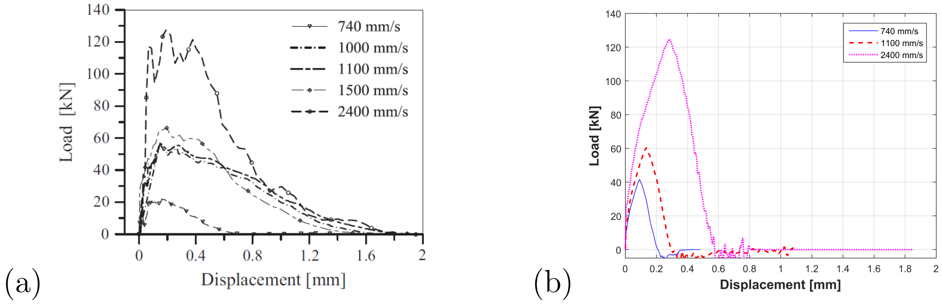

FIGURE 11: Experimental load-displacement response (Ozbolt et al., 2015) for applied velocities larger than 740 mm/s (a) and corresponding numerical curves for three displacement rates (b).

developing more distributed failure. This could be linked with the capacity of the model to induce rate-type viscous damage regularization for the mesh dependency and the fact that this regularization is less effective at low rates of loading.

With the increase of the applied velocity, the failure mode changes from the opening mode to the shear mode. The macroscopic crack path is approaching progressively the loading direction, which corresponds to the classical mode II fracture.

A second feature, already observed in the previous example, is the branching of the main crack for $v = 2.4\,m/s$. As in the compact tension test, we remark the relatively good agreement between experimental and simulation results concerning the branched fracture paths.

In Fig. 11 the experimental load-displacement curves (Ozbolt et al., 2015) and the corresponding numerical repsonse for $v = 0.74\,m/s$, $v = 1.1\,m/s$ and $v = 2.4\,m/s$ are given. Similitudes between numerical and experimen-

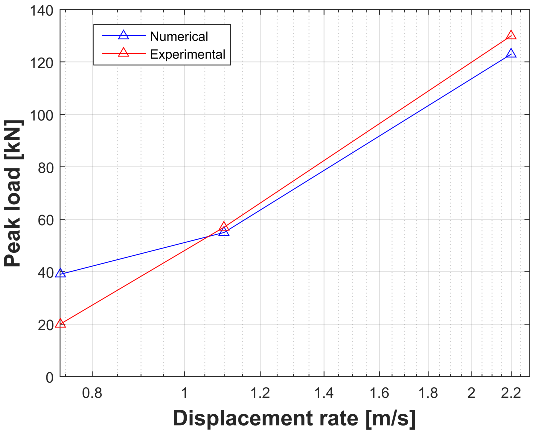

Figure 12: Numerical and experimental values of the peak loads vs the loading rate for the L-specimen test.

tal curves can be noticed for the peak values, while the softening regimes are quite different. Supplementary ingredients should be incorporated in the model to also retrieve the experimental behavior close to complete failure.

It can be observed that the peak load increases with the applied displacement rate and its numerical values are close to the experimental ones. In Fig. 12, the peak load obtained for the three velocities is plotted as a function of the corresponding displacement rate in logarithmic scale together with the experimental values reported in Ozbolt et al. (2015). As in the case of the compact tension test, while for low velocities some difference can be noticed, for higher loading rates measured and computed values are in good agreement.

In order to illustrate the influence of the size of the FE mesh elements on the damage simulations we give in Fig. 13 the failure paths for two meshes with element sizes of $2.5\,mm$ and $1.25\,mm$, respectively, in the case of the

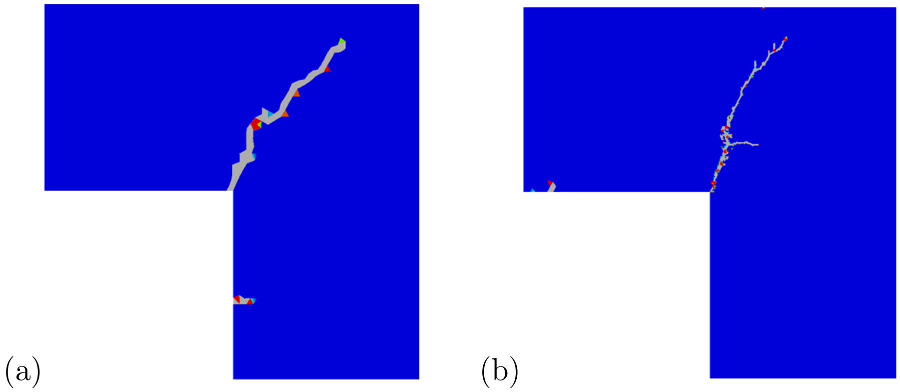

Figure 13: Mesh independence of L-shaped specimen test : a) element size $= 2.5\,mm$ and b) element size $= 1.25\,mm$.

loading speed $v = 740\,mm/s$. Rather similar crack evolutions can be observed, with only a slight deviation induced by a branching event. The mesh size has small influence on damage evolution and this is also true for the peak load values that are close to the ones in Fig. 12.

5. Compact compression specimen test

The third example we consider is the compact compression specimen (CCS) test. Following the experiments reported in Rittel and Maigre (1996a,b), we simulate the mixed-mode dynamic crack initiation and propagation in a PMMA sample under impact loading. The geometry of the specimen is represented in Fig. 14a, the major dimensions being $60\,mm$ of width and $70\,mm$ of height. It contains two notches of dimensions : $1\,mm \times 16\,mm$ and $20\,mm \times 35\,mm$, with semicircular tips. The impact is modeled as an applied velocity over a region of $16.5\,mm$ long on the bottom left side, corresponding to the diameter of the Hopkinson bar used in the experiment.

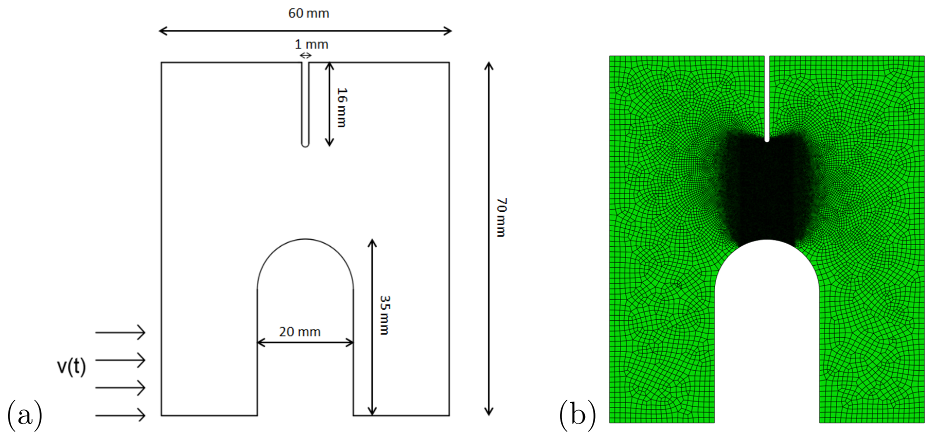

FIGURE 14: Geometry (a) and mesh (b) used in the simulations of the CCS test.

The PMMA material parameters are those reported in the experiments : the dynamic Young modulus $E = 5.76\,GPa$, the Poisson ratio $\nu = 0.42$, the mass density $\rho = 1180\,kg/m^3$ and the fracture energy of $\mathcal{G}_c = 350\,J/m^2$. The calibrated microstructural length is $\epsilon = 3.5e^{-4}\,m$.

Simulations are performed in the Abaqus/Explicit code on a two-dimensional domain discretized with plane strain 4-node bilinear elements with reduced integration and hourglass control. A typical finite element mesh is shown in Fig.14b with the approximate element size of $0.08\,mm$.

The computed fracture paths are illustrated in Fig. 15. Depending on the value of the impact velocity v, the crack initiation angles with respect to the vertical direction are different. For $v = 10\,m/s$ the failure initiation takes place at an angle of 26^0, while for $v = 20\,m/s$ the damage computations provide a higher angle of 62^0. These results are in perfect agreement with those measured in the experiments by Rittel and Maigre (1996a). These authors have found an initial crack angle of $20^0 - 22^0$ for $v = 10\,m/s$ and

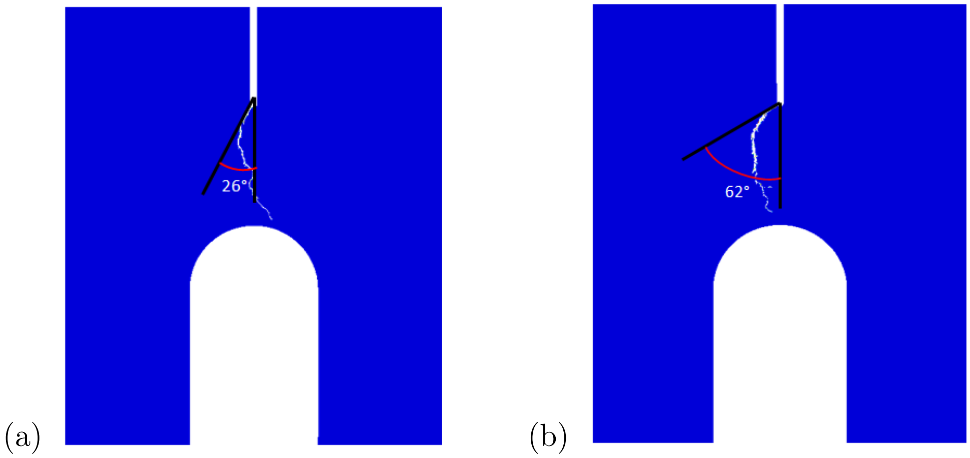

FIGURE 15: Fracture paths with their initiation angle for the CCS test with impact velocities : (a) $v = 10\,m/s$, (b) $v = 20\,m/s$.

$Velocity$	$Experiment$	$Simulation$
$10\,m/s$	$20^0 - 22^0$	26^0
$20\,m/s$	$61^0 - 62^0$	62^0

TABLE 1: Kinking angles measured by Rittel and Maigre (1996a) and predicted values in the numerical simulations of the CCS test.

of $61^0 - 62^0$ for the impact velocity $v = 20\,m/s$. These experimental and simulation results are reported in Table 1. The two-scale damage model shows good prediction capacity concerning the fracture initiation direction in the CCS test on PMMA samples.

In order to illustrate the role of the inertial effects, accounted by the damage model, we represented in Fig. 5 the evolution of the kinetic energy

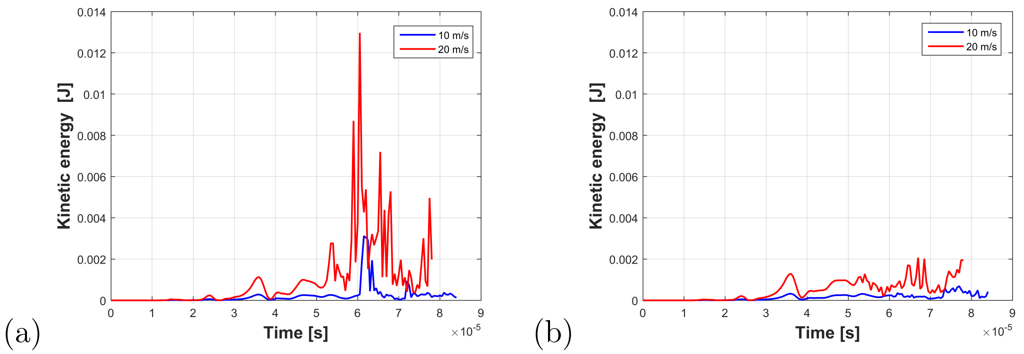

FIGURE 16: Kinetic energy vs time in a damaged element a) and in a neighbor undamaged element b) for two impact velocities.

in two neighbor elements of the Finite Element mesh for the impact velocities $v = 10\,m/s$ and $v = 20\,m/s$. The left figure a) corresponds to a damaged element while the right one b) to an undamaged element. The corresponding damage dissipation $Y.\dot{d}$ in the damaged element, integrated over a time step of $1e - 10\,s$ is shown in Fig. 5 for the two applied velocities.

We note a substantial increase of the kinetic energy accompanying the damage evolution, as a consequence of the microscopic inertial effects around the microcrack lips. The comparison with the undamaged element clearly shows that the origin of this particular evolution is the microcrack growth. The peak value of the kinetic energy corresponds to the time the the element is damaged. For high impact velocities, these inertial effects are amplified.

In Fig. 18, simulations of the CCS test are presented for two mesh element sizes : $0.16\,mm$ and $0.08\,mm$, under the impact velocity of $v = 10\,m/s$. The failure paths are represented in a small region close to the pre-existing notch tip. Despite the different microbranching patterns, we can remark that

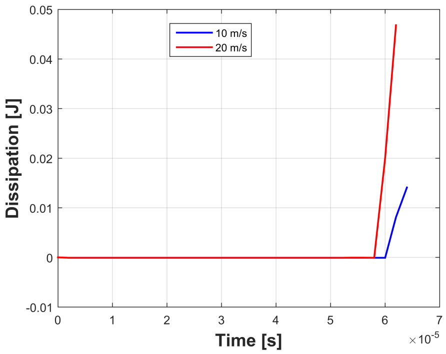

FIGURE 17: Dissipation vs time in a damaged element and on a time step of 1e-10 s, for two impact velocities.

the kinking angles with respect to the notch direction are similar, with a value of about 26^0.

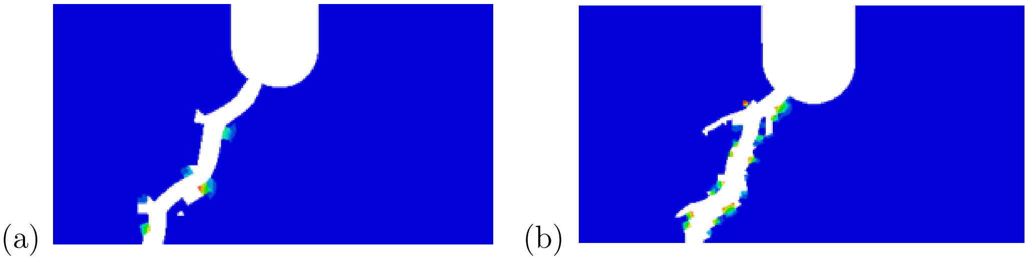

FIGURE 18: Compact compression specimen test simulations for two FE meshes with a) element size $= 0.16\,mm$ and b) element size $= 0.08\,mm$.

6. LECEI test on limestone specimens

In this last example we attempt to model the Loading Edge Cracks by Edge Impact (LECEI) test on Solnhofen limestone rock described in Bertram

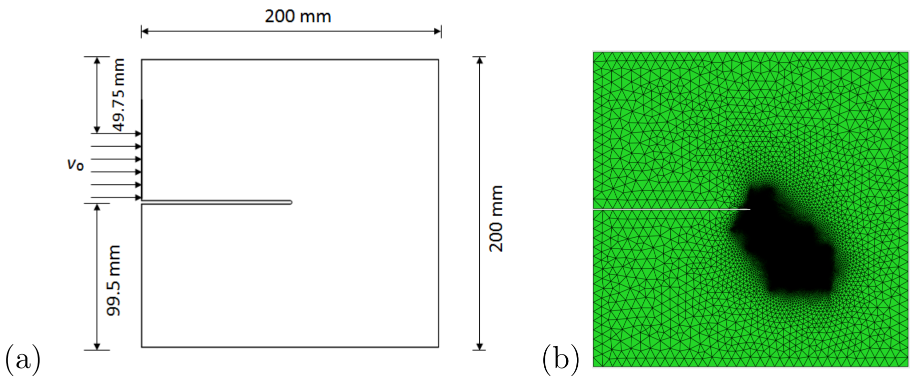

FIGURE 19: Geometry and loading (a) and FE mesh (b) for the LECEI test.

and Kalthoff (2003); Bertram (2008). A specimen with an edge notch is submitted to a impact shear loading and develops mode I failure in a direction inclined with respect to that of the notch and the impactor.

A schematic representation of the LECEI experiment is given in Fig. 19a. The specimen dimensions are $200\,mm \times 200\,mm$, with an initial notch of length $100\,mm$ and width $1\,mm$ having a rounded tip of semicircular shape. A constant velocity v_0 is applied on half of the left upper part, initiating a compressive wave that produces a shear loading state at the tip of the notch.

The Solnhofen limestone material properties are those reported in the experiments : Young's modulus $E = 62\,GPa$, Poisson's ratio $\nu = 0.3$, mass density $\rho = 2600\,kg/m^3$ and fracture energy $\mathcal{G}_c = 14.7\,J/m^2$. The microstructural length used for the computations is $\epsilon = 8e^{-6}\,m$.

The computations are performed under plane stress conditions in the Abaqus/Explicit code, with linear triangular elements of approximate size $2e^{-5}\,m$. Such a mesh is presented in Fig. 19b.

In order to estimate the influence of the impact velocity v_0 on the failure

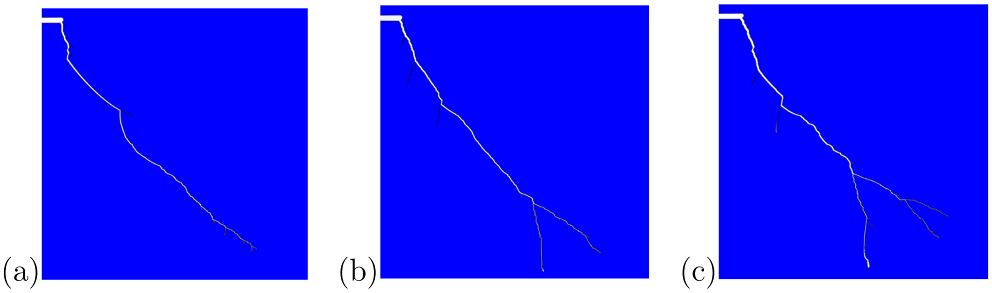

FIGURE 20: Crack patterns of LECEI test corresponding to impact velocities : (a) $v_0 = 12\,m/s$, (b) $v_0 = 15\,m/s$, (c) $v_0 = 18\,m/s$.

mode, simulations were performed for the values $v_0 = 12\,m/s$, $v_0 = 15\,m/s$ and $v_0 = 18\,m/s$. The resulting crack paths over a period of $40\mu s$ are presented in Fig.20. A mode I crack is formed and propagates in the lower part of the specimen. It can be remarked that for the small impact velocity a single crack is formed, while for the higher velocity multiple branchings are developed. This multi-branch fracture system corresponds well to the experimental observations reported in Bertram and Kalthoff (2003); Bertram (2008) and reproduced in Fig. 21.

For a more precise comparison between the model predictions and experiments, we present in Fig.21 the failure evolution events from Bertram and Kalthoff (2003); Bertram (2008) and the corresponding states obtained by simulations with the present damage model, over a time interval of $40\mu s$. We remark the good correspondance between the two series of fracture events over the whole time range, from the early stages with a single main crack to the multiple-branches crack system formed when approaching $t = 40\mu s$.

The damage paths obtained by simulations of the LECEI test with two FE meshes of element size : a) $2e^{-5}\,m$ and b) $1e^{-5}\,m$ are given in Fig. 22. The

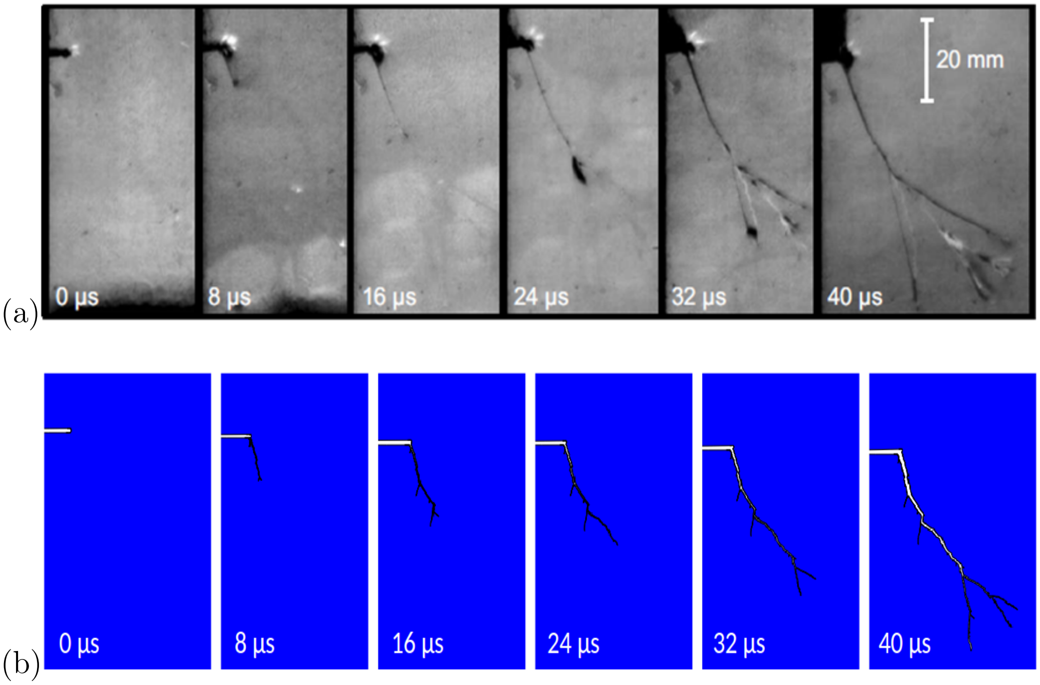

FIGURE 21: Crack propagating events in LECEI test on limestone rocks : (a) experimental images from Bertram and Kalthoff (2003); Bertram (2008) and (b) FE simulations with the two-scale damage model.

refinement of the mesh has not important effects on the damage evolution and the main branching events occur in similar way in the two simulations.

7. Conclusions

A two-scale model of damage, based on the dynamic mode I evolution of microcracks, has been used to simulate dynamic failure experiments like the compact tension and L-shaped specimen tests for concrete, the compact compression test for the PMMA polymer and the LECEI test on brittle limestone rocks. The analysis focused on the influence of the loading rate on

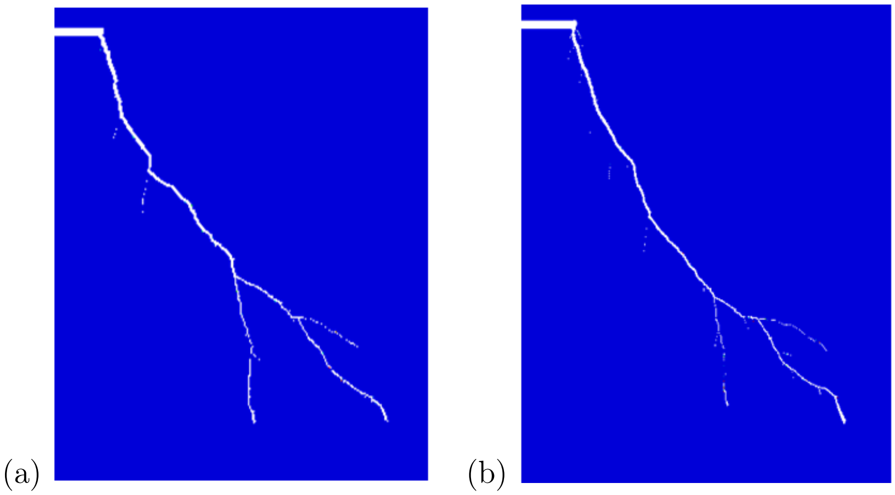

FIGURE 22: Simulations of the LECEI test with two FE meshes of element size : a) $2e^{-5}\,m$ and b) $1e^{-5}\,m$.

the failure mode, with different crack trajectories and branching effects, by comparing the model predictions with the experimental results.

The model has been implemented in the commercial Finite Element code Abaqus/Explicit and simulations of the dynamic failure tests have been performed in two or three-dimensional framework.

The results of the computations for the compact tension and L-specimen tests showed that for low loading rates the fracture path is approximately in the opening mode, while for higher applied velocities it switches to a mixed mode, with a tendency of approaching the mode II and with associated crack branching effects. This specific influence of the loading rate has been observed experimentally and it was retrieved in the present simulations.

Computations for the compact compression test allowed us to evaluate the influence of the impact velocity on the crack initiation angle. It has been shown that the kink angle increases with the value of the applied velocity and that the obtained numerical results are in agreement with those reported in the experiments.

The development of mode I fracture under shear loading has been studied for the Kalthoff's LECEI test on brittle rocks. In this last example, the analysis concerned the development of the multi-crack system as the result of branching of the main crack at high impact loadings. Comparison with experimental images showing the failure evolution over the whole time range provided good correspondence with the simulation results.

A study of the mesh size dependence of the FE simulations has been performed for each test considered and the results showed relatively small influences. The main failure modes have been obtained independently of the mesh, for sufficiently small element sizes.

The four tests considered in the present contribution, involving different types of loading, failure modes and constitutive materials, allowed us to evaluate the prediction capacity of the two-scale damage model. The essential experimental features concerning the effects of the loading rate on dynamic failure have been retrieved in the simulations.

Despite the fact that the model is based only on mode I microcrack growth, macroscopic mixed-mode dynamic fracture effects have been correctly reproduced. Further improvements of the present model may include the incorporation of the mixed mode propagation at the microscopic scale.

References

ABAQUS 6.13, Analysis User's Manual. Dassault Systemes Simulia Corporation, RI, USA, (2013).

O. Allix, P .Feissel, P .Thévenet, A delay damage mesomodel of laminates under dynamic loading : basic aspects and identification issues. Computers and Structures, 81 (2003) 1177-1191.

N.P. Banthia, S. Mindess, A. Bentur, Impact behavior of concrete beams. Materials and Structures, 20 (1987) 293-302.

N. Bede, J. Ozbolt, A. Sharma, B. Irhan, Dynamic fracture of notched plain concrete beams : 3D finite element study. International Journal of Impact Engineering, 77 (2015) 176-188.

A. Bertram, J.F. Kalthoff, Crack propagation toughness of rock for the range from low to very high crack speeds, Key Engineering Materials, 251-252 (2003) 423-430.

A. Bertram, Bruchenergie Laufender Risse in Gestein, Dissertation Ruhr-University, Bochum, (2008).

A. Brara, J.R. Klepaczko, Experimental characterization of concrete in dynamic tension. Mechanics of Materials, 38 (2006) 253-267.

P.H. Bischoff, S.H. Perry, Compressive behavior of concrete at high strain rates. Materials and Structures, 24 (1991) 425-450.

C. Dascalu, Multiscale modeling of rapid failure in brittle solids : branching instabilities. Mechanics of Materials, 199 (2018) 2765-2778.

C. Dascalu, Dynamic localization of damage and microstructural length influence. International Journal of Damage Mechanics, 26 (2017) 1190-1218.

C. Dascalu, B. François, O. Keita, A two-scale model for subcritical damage propagation. International Journal of Solids and Structures, 47 (2010) 493-502.

C. Dascalu, A two-scale damage model with material length. Comptes Rendus-Mécanique, 337 (2009) 645-652.

C. Dascalu, G. Bilbie, Agiasofitou E., Damage and size effect in elastic solids : a homogenization approach. International Journal of Solids and Structures, 45 (2008) 409-430.

A. Dobrovat, C. Dascalu, S. Hall, Computational modeling of damage based on micro-crack kinking. International Journal for Multiscale Computational Engineering, 13 (2015) 201-217.

J.F. Dubé, G. Pijaudier-Cabot, C. La Borderie, Rate dependent damage model for concrete in dynamics. Journal of Engineering Mechanics, 122 (1996) 939-947.

B. Erzar, P. Forquin, Analysis and modeling of the cohesive strength of concrete at high strain-rates. International Journal of Solids and Structures, 51 (2014) 2559-2574.

D. Fanella, D. Krajcinovic, A micromechanical model for concrete in compression. Engineering Fracture Mechanics, 29 (1988) 49-66.

B. François, C. Dascalu, A two-scale time-dependent damage model based on non-planar growth of micro-cracks, Journal of the Mechanics and Physics of Solids, 58 (2010) 1928-1946.

P. Forquin, B. Erzar, Dynamic fragmentation process in concrete under impact and spalling tests. International Journal of Fracture, 163 (2010) 193-215.

L.B. Freund, Dynamic Fracture Mechanics. Cambridge University Press, (1998).

J.R. Klepaczko, A. Brara, An experimental method for dynamic tensile testing of concrete by spalling. International Journal of Impact Engineering, 25 (2001) 387-409.

O. Keita, C. Dascalu, B. François, A two-scale model for dynamic damage evolution. Journal of the Mechanics and Physics of Solids, 64 (2014) 170-183.

K. Kirane, Y. Su, Z.P. Bazant, Strain-rate dependent microplane model for high-rate comminution of concrete under impact based on kinetic energy release theory. Proceedings of the Royal Society, A 471 (2015) 20150535.

M. Larcher, Development of discrete cracks in concrete loaded by shock waves. International Journal of Impact Engineering, 36 (2009) 700-710.

R.J. Malvar, C.A. Ross, Review of strain rate effects for concrete in tension. ACI Materials Journal, 95 (1998) 735-739.

X. Markenscoff, C. Dascalu, Asymptotic homogenization analysis for damage amplification due to singular interaction of microcracks. Journal of Mechanics and Physics of Solids, 60 (2012) 1478-1485.

T. Menouillard, J. Rethore, N. Moes, A. Combescure, H. Bung, Mass lumping strategies for X-FEM explicit dynamics : application to crack propagation. International Journal for Numerical Methods in Engineering, 74 (3) (2008) 447-474.

C. Miehe, M. Hofacker, F. Welschinger, A phase field model for rate-independent crack propagation : Robust algorithmic implementation based on operator splits. Computer Methods in Applied Mechanics and Engineering, 199 (2010) 2765-2778.

J. Ozbolt, K.K. Rah, D. Mestrovic, Influence of loading rate on concrete cone failure. International Journal of Fracture, 139 (2006) 239-252.

J. Ozbolt, A. Sharma, Numerical simulation of dynamic fracture of concrete through uniaxial tension and L-specimen. Engineering Fracture Mechanics, 85 (2012) 88-102.

J. Ozbolt, J. Bosnjak, E. Sola, A two-scale time-dependent model of damage : Dynamic fracture of concrete compact tension specimen : Experimental and numerical. International Journal of Solids and Structures, 50 (2013) 4270-4278.

J. Ozbolt, N. Bede , A. Sharma, A. Mayer, Dynamic fracture of concrete L-specimen : Experimental and numerical study. Engineering Fracture Mechanics, 148 (2015) 27-41.

H.W. Reinhardt, Concrete under impact loading tensile strength and bond. Heron, 27 (3) (1982) 1-48.

X. Ren, J. S. Chen, J. Li, T. R. Slawson, M. J. Roth, Micro-cracks informed damage models for brittle solids. International Journal of Solids and Structures, 48 (2011) 1560-1571.

D. Rittel, H. Maigre, A study of mixed-mode dynamic crack initiation in PMMA. Mechanics Research Communications, 23 (5) (1996) 475-481.

D. Rittel, H. Maigre, An investigation of dynamic crack initiation in PMMA. Mechanics of Materials, 23 (3) (1996) 229-239.

J. Weerheijm, J.C.A.M. Van Doormaal, Tensile failure of concrete at high loading rates : New test data on strength and fracture energy from instrumented spalling tests. International Journal of Impact Engineering, 34 (2007) 609-626.

A. Wrzesniak, C. Dascalu, P. Besuelle, A two-scale time-dependent model of damage : Influence of micro-cracks friction. European Journal Mechanics A-Solids, 49 (2015) 345-361.